



Cite this: *New J. Chem.*, 2020, **44**, 18489

Received 19th April 2020,
Accepted 2nd August 2020

DOI: 10.1039/d0nj01955k

rsc.li/njc

Transition metal sulfide-laminated copper wire for flexible hybrid supercapacitor†

Swati J. Patil,^{ib}ab R. B. Pujari,^a Tian-Feng Hou^a and Dong-Weon Lee^{ib}*ac

In this paper, we propose a flexible wire-type hybrid supercapacitor (FWHSC) endowed with superior electrochemical properties of transition metal sulfide nano-flakes. The electrodeposition method was conducted for coating of electroactive transition metal sulfide (CoS, NiCo₂S₄, CoS/NiCo₂S₄ and ZnCo₂S₄) nanomaterials on the current collector (Cu-wire), which makes it possible to store the electrochemical energy. The electrochemical study of NiCo₂S₄ and ZnCo₂S₄ electrodes revealed excellent charge storage features with areal capacitance of 245.5 and 104.6 mF cm⁻², respectively, at a scan rate of 2 mV s⁻¹. The FWHSC assembled from Cu@CoS/NiCo₂S₄ and Cu@ZnCo₂S₄ electrodes and KOH/PVA gel electrolyte operates in a voltage range of 1.5 V and delivers a specific energy of 6 W h kg⁻¹ at the specific power of 4500 W kg⁻¹ and a cycling stability of over 2000 cycles.

Introduction

Energy storage devices are being investigated not only for their high energy storage capacity, but also for their attractive characteristics like rapid charge/discharge rates and long-term cycling life span. The unprecedented growth of portable and wearable electronic devices in recent years has encouraged scientists and engineers to come up with novel ideas for flexible, smart, safe, and simultaneously efficient devices.^{1–3} The flexibility and lightweight features of modern energy storage systems are more important in order to use in wearable devices.⁴ Flexible supercapacitors are versatile energy storage devices for mobile and flexible electronics owing to their high energy density, high-speed charging capacity, light-weight, small volume, and large number of charging and discharging cycles.^{5–7} Energy storage in supercapacitors can be achieved by either electrostatic two-layer ion adsorption–desorption or reversible and fast faradaic redox reactions that make supercapacitors the most suitable candidate for portable electronic devices with high energy power density.⁸

Recently, high-performance wire-shaped flexible supercapacitors have been investigated for portable applications. Until now, stainless steel,⁹ Ti,¹⁰ Ni,¹¹ Au,¹² and Cu¹³ materials have been used as current collectors with great interest to improve the energy storage capability in limited space during the fabrication

of wire-shaped supercapacitors. Transition metal oxides, as well as metal sulfides, including RuO₂, MnO₂, Ni(OH)₂, Co(OH)₂, NiS, Fe₂O₃, CoS, and MnS, offer influential assortment of electrochemical electrode materials for abundant reversible redox reactions and good theoretical capacity.^{14–18} However, bulky metal oxide or sulfide distribution of the material may cause mediocre electrochemical performance due to limited functionality and electrostatic surface area.¹⁹ To overcome these limitations, binary transition metal sulfides have been extensively investigated as alternative faradaic electrode materials. The appropriate tripartite sulfides MCo₂S₄ (M = Ni²⁺, Mn²⁺, Zn²⁺, and Cu²⁺) exhibit a synergistic effect on faradaic interactions by introducing an individual metal element.^{20,21} In addition, replacement of oxygen with sulfur leads to the formation of a more flexible and easy structure.²²

Herein, we used Cu-wire as the supporting substrate, and a simple one-step electrodeposition route was followed for the nanostructured material preparation. In order to use these two different materials in the actual application, it was important to create an energy storage device with a basic configuration. Therefore, the charge storage kinetics and surface contribution analyses of Cu@CoS/NiCo₂S₄ and Cu@ZnCo₂S₄ material electrodes in the field of energy storage systems were evaluated with the power-law relation. Finally, a wire-type hybrid supercapacitor device was fabricated and its electrochemical features were tested at different bending angles.

Results and discussion

Morphological and structural characterizations

The surface morphologies and microstructures of the prepared materials were investigated by the field emission scanning electron microscopy (FE-SEM) technique. The obtained results

^a MEMS and Nanotechnology Laboratory, Graduate School of Mechanical Engineering, Chonnam National University, Gwangju 61186, Republic of Korea. E-mail: mems@jun.ac.kr

^b Department of Energy and Materials Engineering, Dongguk University-Seoul, Seoul, 04620, Republic of Korea

^c Center for Next-Generation Sensor Research and Development, Chonnam National University, Gwangju 61186, Republic of Korea

† Electronic supplementary information (ESI) available. See DOI: 10.1039/d0nj01955k

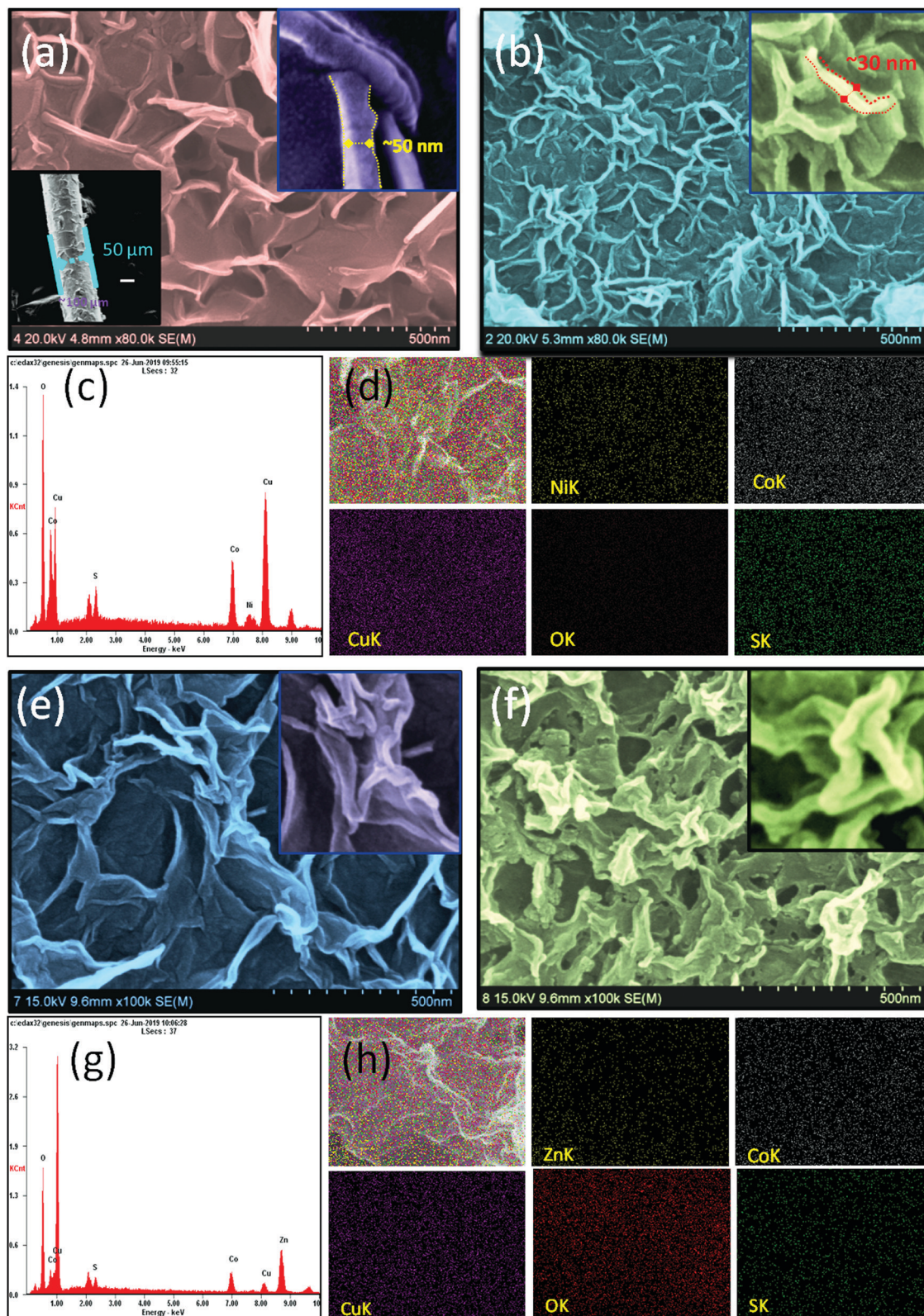


Fig. 1 SEM images of (a) Cu@CoS, (b) Cu@NiCo₂S₄, (e) Cu@CoS/NiCo₂S₄ and (f) Cu@ZnCo₂S₄ and insets (top) show the HR-SEM images of the respective materials. SEM image of single Cu-wire shown inset (bottom) of (a). EDX spectrum (c and g) and related elemental mapping (d and h) of the Cu@CoS/NiCo₂S₄ and Cu@ZnCo₂S₄ materials.

for Cu@CoS, Cu@NiCo₂S₄, Cu@CoS/NiCo₂S₄, and Cu@ZnCo₂S₄ materials were electro-deposited on Cu-wire. Inset of Fig. 1(a) are displayed in Fig. 1(a), (b), (e) and (f), respectively. The (bottom) shows the SEM image of Cu-wire at low-magnification

with a wire thickness of about 100 μm . Further, a single layer of CoS and NiCo_2S_4 was electro-deposited on the Cu-wire separately, and the obtained surface nanostructures are shown in Fig. 1(a) and (b), respectively. The surface morphologies of CoS and NiCo_2S_4 have nanoflake-like nanostructures with a flake width of nearly 50 and 30 nm, respectively. For the bimetallic electrode, the size of the flakes decreased and a porous interconnected network was observed. Fig. 1(e) exhibits the surface morphology of $\text{Cu@CoS/NiCo}_2\text{S}_4$ hybrid electrode. It is clearly observed in Fig. 1(e) that $\text{Cu@CoS/NiCo}_2\text{S}_4$ exhibits thin transparent nanoflakes with porous and uniformly deposited surface nanostructure as compared to CoS and NiCo_2S_4 . The surface morphological view is seen in Fig. 1(f) for electrodeposited ZnCo_2S_4 on Cu-wire. An interwoven discrepant surface with tiny nanostructures was observed for $\text{Cu@ZnCo}_2\text{S}_4$. The insets (top) of Fig. 1(a, b, e and f) show magnified SEM images of Cu@CoS , $\text{Cu@NiCo}_2\text{S}_4$, $\text{Cu@CoS/NiCo}_2\text{S}_4$, and $\text{Cu@ZnCo}_2\text{S}_4$ materials, respectively. Further, energy-dispersive X-ray spectroscopy (EDX) was employed for the elemental composition analysis and elemental mapping of the electrodeposited materials. Fig. 1(c) represents the EDX spectra of $\text{Cu@CoS/NiCo}_2\text{S}_4$ and the corresponding elemental map of Ni, Co, Cu, O and S are given in Fig. 1(d). EDX spectra and elemental distribution shown in Fig. 1(h) have identified the presence of Zn, Co, Cu, O elements in the $\text{Cu@ZnCo}_2\text{S}_4$ sample (Fig. 1(g)). The atomic percentages of the electrodeposited materials are provided in the ESI,[†] Table S1. Thus, EDX results confirmed that the molar ratio of Ni:Co:S in the nanoflakes and Zn:Co:S in the nanosheets was nearly 1:2:4, which further proved the hierarchical nanostructures on the Cu-wire surface. Moreover, the surface oxy-groups are present in the samples. Meanwhile, the synergistic advantages of the nanostructure composition and

porous interconnected network enhanced the electrochemical performances of $\text{Cu@CoS/NiCo}_2\text{S}_4$ and $\text{Cu@ZnCo}_2\text{S}_4$ materials as it underwent the continuous ion exchange process and electrochemical measurements. X-ray diffraction (XRD) studies were carried out for the crystallographic analysis of the electrodeposited samples. The XRD patterns of $\text{Cu@CoS/NiCo}_2\text{S}_4$ and $\text{Cu@ZnCo}_2\text{S}_4$ provided in Fig. S1 (ESI[†]) were obtained in the scan range of 10–80°. The observed peaks at 43.29°, 50.43° and 74.13° can be attributed to copper wire, which are in good agreement with cubic Cu (JCPDS No. 00-004-0836). It is clear that apart from peaks corresponding to Cu-wire, none of the diffraction peaks of NiCo_2S_4 and ZnCo_2S_4 material were observed due to the low thickness and nanocrystalline nature of the electrodeposited material.

To draw insights into the surface composition and valence states of the elements of $\text{Cu@CoS/NiCo}_2\text{S}_4$ and $\text{Cu@ZnCo}_2\text{S}_4$ samples, the X-ray photoelectron spectra (XPS) were obtained. Fig. S2 (ESI[†]) shows the wide XPS spectra of CoS/ NiCo_2S_4 and ZnCo_2S_4 materials and the core level spectrum of Cu 2p. The XPS profile revealed the presence of Ni 2p, Co 2p, and S 2p states in CoS/ NiCo_2S_4 (Fig. 2(a–c)). Zn 2p, Co 2p, and S 2p core level energy states of ZnCo_2S_4 , are seen in Fig. 2(d–f). The two Gaussian peaks in each spectrum indicate the divalent states of Cu^{2+} , $^{23}\text{Ni}^{2+}$, $^{24}\text{Zn}^{2+}$, and Co^{2+26} presented in CoS/ NiCo_2S_4 and ZnCo_2S_4 . Interestingly, the XPS peaks observed at 163.2 and 162.4 eV in the spectra of CoS/ NiCo_2S_4 and ZnCo_2S_4 materials are characteristic of the S^{2-} state of sulfur.²⁷ Another peak observed in the range of 165–169 eV can be ascribed to sulphur and oxygen bonding, caused by air exposure.²⁸

Electrochemical studies

The comparative cyclic voltammograms (CVs) of CoS, NiCo_2S_4 , CoS/ NiCo_2S_4 and ZnCo_2S_4 electrodes recorded at 50 mV s^{-1}

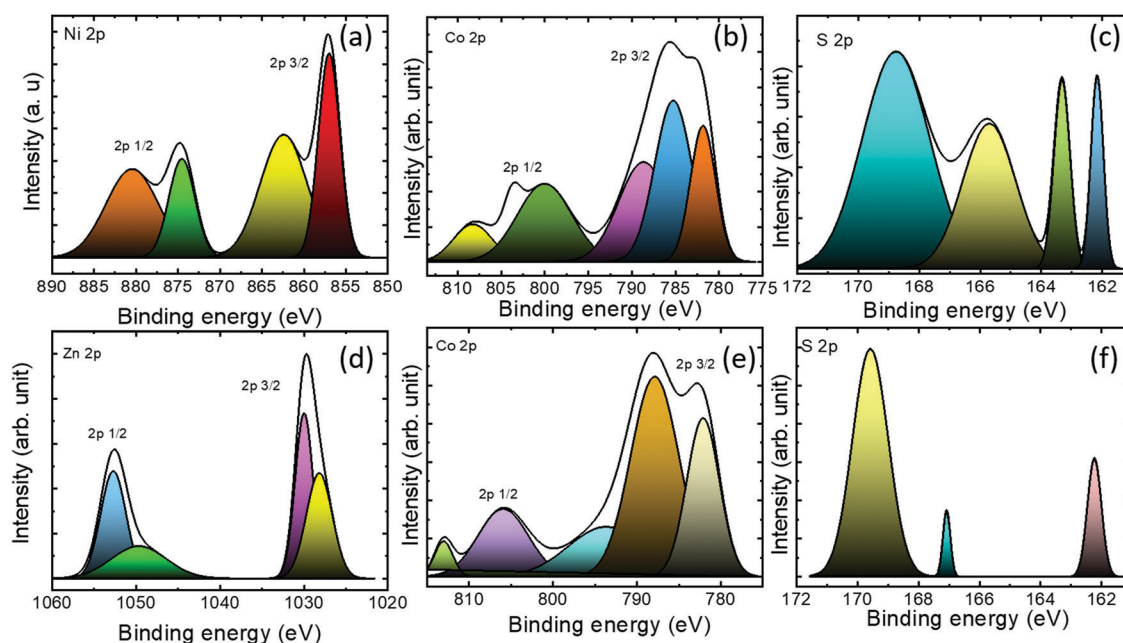


Fig. 2 The core-level XPS spectra of (a–c) Ni 2p, Co 2p, and S 2p states presented in $\text{Cu@CoS/NiCo}_2\text{S}_4$, and the core-level spectra of (d–f) Zn 2p, Co 2p, and S 2p state present in $\text{Cu@ZnCo}_2\text{S}_4$.

scan rate are shown in Fig. 3(a). The Cu@CoS@NiCo₂S₄ electrode exhibits the highest current density due to the influence of the double layer of CoS and bimetallic cations from NiCo₂S₄. A pair of redox peaks was observed in the CV of Cu@CoS/NiCo₂S₄, which demonstrated excellent faradaic properties of the electrodeposited material as observed in Fig. 3(b). It arises from the reversible Ni³⁺/Ni²⁺ redox couple in KOH electrolyte and is more evident at lower scan rates. The slight shift of the cathodic and anodic peaks in the positive and negative sides as a function of scan rate indicates the charge storage kinetics of the Cu@CoS/NiCo₂S₄. Fig. 3(c) shows the cyclic voltammetry response of the Cu@ZnCo₂S₄ electrode at different scan rates representing the redox reactions related to the Co⁴⁺/Co³⁺ couple. The shape of CV curves did not change significantly with increasing the scan rate from 2 to 100 mV s⁻¹, indicating a good electrochemical reversibility of the electrodeposited material. Laterally, the effect of scan rates on the CV response of Cu@CoS, Cu@NiCo₂S₄, Cu@ZnCo₂S₄, and Cu@CoS/NiCo₂S₄ electrodes are presented in Fig. 3(d). As a function of the

scan rate, the areal capacitance values for Cu@CoS/NiCo₂S₄ electrode were calculated to be 245.43, 186.40, 172.55 and 152.12 mF cm⁻² at 2, 10, 50 and 100 mV s⁻¹ scan rates, respectively. Similarly, the calculated areal capacitances of 104.52, 82.3, 64.7 and 58 mF cm⁻² correspond to the scan rates of 2, 10, 50 and 100 mV s⁻¹, respectively, for the Cu@ZnCo₂S₄ electrode. It indicates that the faradaic redox reactions are limited as the scan rate increases due to the inadequate response of the ions in the electrolyte to the active material, resulting in less effective interactions between them at higher scan rates. However, faradaic redox reactions involving pseudocapacitive materials are not restricted to the distribution of ions. On the other hand, battery-type materials are diffusion-controlled, where the pseudocapacitor reflects the maximum power strength. According to the power-law formula (eqn (1)), this can be determined by analyzing the peak current of CV curves at lower scan rates.²⁹

$$i = av^b \quad (1)$$

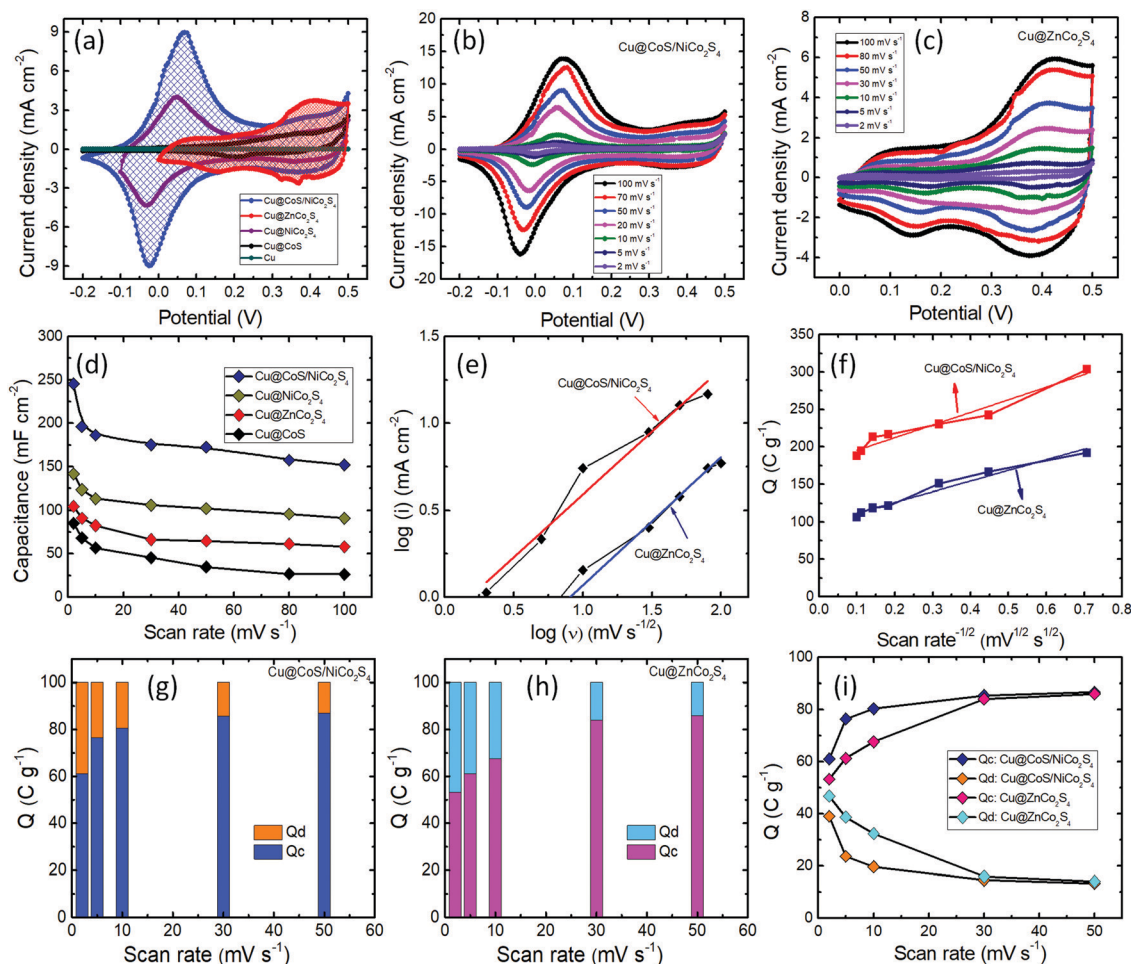


Fig. 3 (a) Comparative CV profiles of different electrodes at 50 mV s⁻¹ scan rate, (b and c) CV curves of the Cu@CoS/NiCo₂S₄ and Cu@ZnCo₂S₄ electrode at various scan rates, (d) areal capacitances calculated from CV curves at different scan rates for all electrodes, (e) plot of logarithmic current density against logarithmic scan rate represents the capacitive property. (f) The calculated total capacity as a function of the inverse scan rate. (g and h) The bar diagram exhibits the determined total charge storage contributions from capacitive and diffusion-controlled processes at lower scan rates for Cu@CoS/NiCo₂S₄ and Cu@ZnCo₂S₄ material electrodes (i).

where a and b are adjustable parameters, i is the peak current of CV curves and ν is the scan rate. The values of b are variable; $b = 0.5$ indicates faradaic, diffusion-controlled battery type behavior. If $b = 1$, it indicates a capacitive, surface controlled non-faradaic type of behavior for the electrode material. As seen in Fig. 3(e), a linear relationship was observed between logarithmic current ($\log i$) and logarithmic scan rate ($\log \nu$) for cathodic sweeps of the CV. The slope of $\log i$ vs. $\log \nu$, i.e. b value of Cu@CoS/NiCo₂S₄ and Cu@ZnCo₂S₄ electrode materials, were determined to be 0.71 and 0.62, respectively, indicating that diffusion-controlled faradaic type charge storage kinetics occurred in the electrode.

The total charge storage capacity of Cu@CoS/NiCo₂S₄ and Cu@ZnCo₂S₄ electrodes was determined with respect to different scanning rates (Fig. 3(f)). Bar diagrams as shown in Fig. 3(g–i) reveal the capacitive contributions to the total capacities of Cu@CoS/NiCo₂S₄ and Cu@ZnCo₂S₄ electrodes at lower scanning rates. The total charge storage capacity of the electrode is distributed into surface process-controlled charge storage behavior referred as non-faradaic redox capacitance (Q_c) and diffusion controlled faradaic capacitance (Q_d). For both electrodes, the capacitive contribution increases with the scanning rate. Q_c and Q_d were estimated to be 61 and 39% for Cu@CoS/NiCo₂S₄ and 52 and 38% for the Cu@ZnCo₂S₄ electrode materials, respectively. These results represent the coexistence of diffusion and capacity-controlled behavior of both electrode materials. It is seen that at a lower scan rate, the diffusion-controlled processes predominate, and at higher scan rates, the capacity-controlled kinetics coexist.

Fig. 4(a) shows the comparative galvanostatic charge–discharge (GCD) profiles of the Cu@CoS/NiCo₂S₄ and Cu@ZnCo₂S₄

electrodes at a constant current density of 5 mA cm^{−2} in 0–0.5 V/SCE. Fig. 4(b and c) illustrate the presence of non-linear charge–discharge plots representing the faradaic behavior of the Cu@CoS/NiCo₂S₄ and Cu@ZnCo₂S₄ electrodes, which is consistent with the CV results. Based on the charge–discharge profiles, the capacitance values of the Cu@CoS/NiCo₂S₄ electrodes were calculated to be 891, 823 and 764 mF cm^{−2} at 5, 10 to 15 mA cm^{−2}, respectively. Even at a high current density of 15 mA cm^{−2}, it still retains 86% of the initial capacitance, demonstrating excellent rate capability. Similarly, the areal capacitances of the Cu@ZnCo₂S₄ electrodes were calculated as 565, 359, and 283 mF cm^{−2} at the current densities of 5, 10 to 15 mA cm^{−2} (Fig. 4(d)). The maximum length capacitance of the Cu@CoS/NiCo₂S₄ and Cu@ZnCo₂S₄ electrode were calculated as $C_1 = 32.5 \text{ mF l}^{-1}$ and $C_1 = 22 \text{ mF l}^{-1}$, respectively. Further, impedance analysis was carried out to study the charge transfer resistance and capacitive behavior of both Cu@CoS/NiCo₂S₄ and Cu@ZnCo₂S₄ electrodes. Nyquist plot (Fig. 4(e)) exhibits a solution resistance (R_s) in the high-frequency region, charge transfer resistance (R_{ct}) in the mid-high frequency region followed by a vertical line ascribed to the Warburg impedance (Z_w) related to the diffusion of the electrolyte ion. The low R_{ct} value and relatively inclined vertical line of the Cu@CoS/NiCo₂S₄ electrode play a crucial role in enhancing the performance of the supercapacitor. The R_s and R_{ct} values of Cu@CoS/NiCo₂S₄ and Cu@ZnCo₂S₄ electrodes were observed to be 1.1 and 3.5 Ω , and 2.6 and 19 Ω , respectively, which are lower than that of the Cu@CoS electrode with R_s : 2.1 and R_{ct} : 60 Ω . The normalized capacitance plots for all three electrodes in Fig. 4(f) show linear response with frequencies for the Cu@CoS/NiCo₂S₄ electrode and exponential nature for the Cu@CoS and

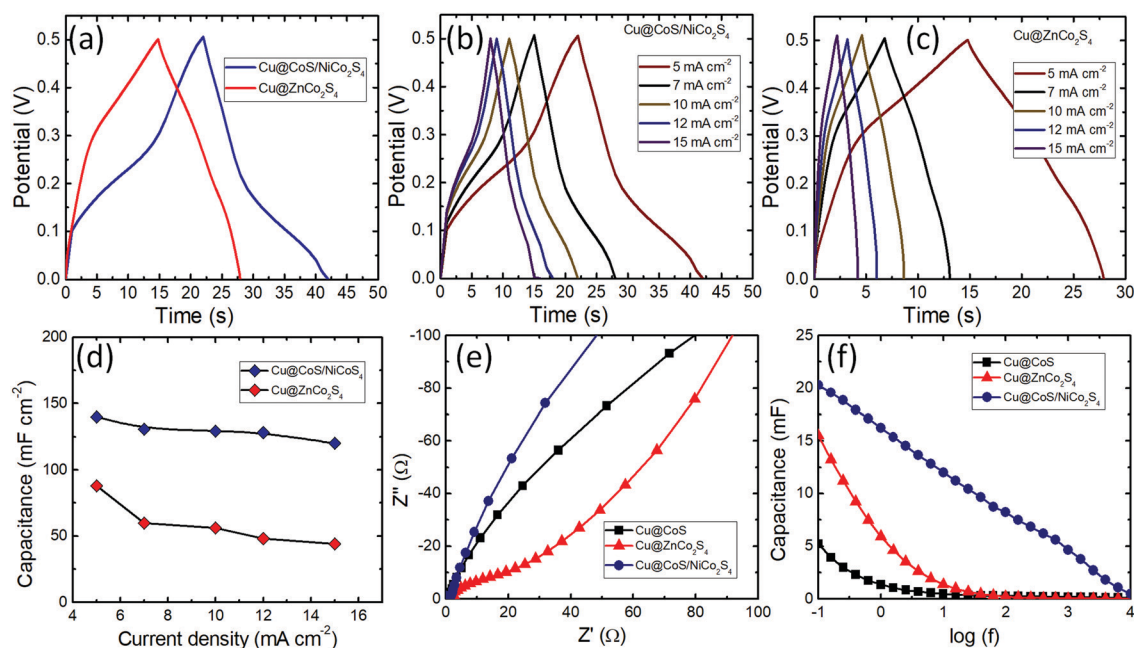


Fig. 4 (a) Comparative charge–discharge curves of the prepared electrodes in the 0 to 0.5 V/SCE potential range. (b and c) GCD curves and corresponding areal capacitances (d) calculated at different current densities for Cu@CoS/NiCo₂S₄ and Cu@ZnCo₂S₄ electrodes. Impedance analysis of Cu@CoS, Cu@CoS/NiCo₂S₄ and Cu@ZnCo₂S₄ electrodes; (e) Nyquist plot, (f) frequency-dependent capacitance.

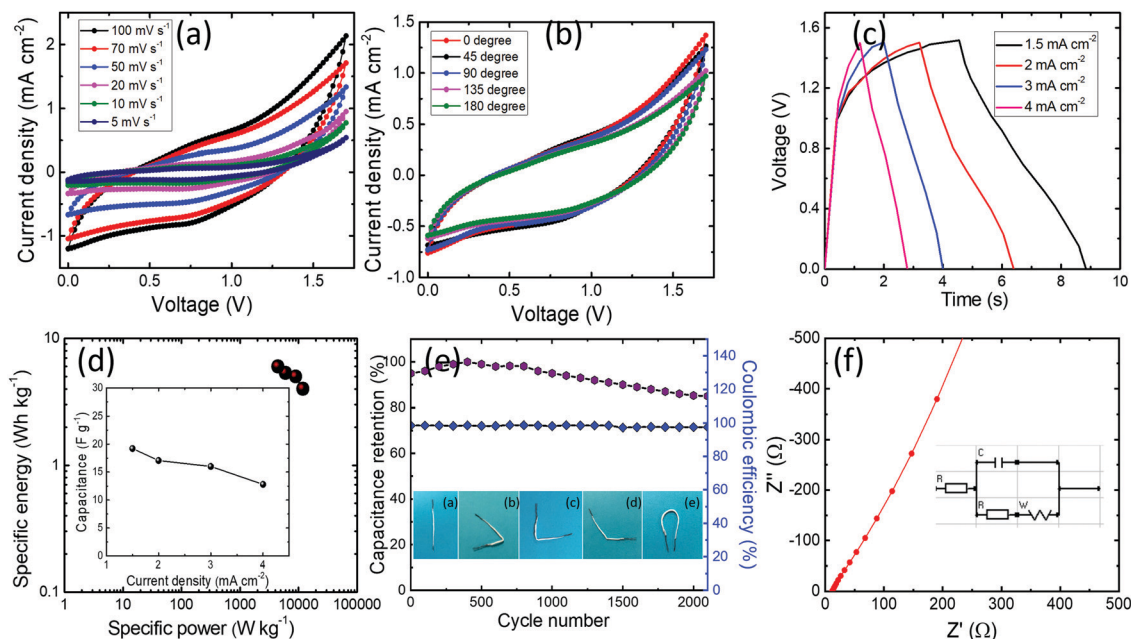


Fig. 5 Electrochemical characterizations of the wire-type $\text{NiCo}_2\text{S}_4//\text{ZnCo}_2\text{S}_4$ FWHSC: (a) typical CV curves at different scanning rates, (b) CV curves with different bending angles at 50 mV s^{-1} scan rate. (c) GCD profiles at 1.5 to 4 mA cm^{-2} current densities, (d) Ragone plot (inset plot presents the specific capacitance against current density). (e) The capacitance retention and coulombic efficiency as a function of cycle number. Inset shows the optical images of the fabricated FWHSC at 0° (i), 45° (ii), 90° (iii), 135° (iv) and 180° (v) bending angle. Impedance analysis; (f) Nyquist plot of the flexible wire-type $\text{NiCo}_2\text{S}_4//\text{ZnCo}_2\text{S}_4$ FWHSC.

$\text{Cu@ZnCo}_2\text{S}_4$ electrodes. Bode plots of Cu@CoS , $\text{Cu@CoS}/\text{NiCo}_2\text{S}_4$ and $\text{Cu@ZnCo}_2\text{S}_4$ electrodes are illustrated in Fig. 4(f), and the corresponding relaxation time constants were calculated as 0.0025 , 0.015 and 0.1 s , respectively.

To investigate the flexibility of the fabricated device, the electrochemical charge storage was evaluated in a two-electrode configuration. The electrochemical properties of the $\text{NiCo}_2\text{S}_4//\text{ZnCo}_2\text{S}_4$ FWHSC device are shown in Fig. 5. Within the optimized voltage range of 1.5 V , the shape of CV curves for the $\text{NiCo}_2\text{S}_4//\text{ZnCo}_2\text{S}_4$ FWHSC device did not change with varying scan rate, which indicates an outstanding electrochemical performance of the device (Fig. 5(a)). $\text{NiCo}_2\text{S}_4//\text{ZnCo}_2\text{S}_4$ FWHSC is highly flexible and easy to bend under different bending angles showing 87% flexibility (Fig. 5(b)) for the highest bending angle of 180° . The optical images of the flexibility test at different angles are shown in the inset of Fig. 5(e). In order to continuously assess the effectiveness of the $\text{NiCo}_2\text{S}_4//\text{ZnCo}_2\text{S}_4$ FWHSC device, GCD measurements (Fig. 5(c)) were recorded at various current densities. The results revealed that the $\text{NiCo}_2\text{S}_4//\text{ZnCo}_2\text{S}_4$ FWHSC device achieves the highest specific capacitance of 19.2 F g^{-1} (4.8 mF cm^{-2}) at 1.5 mA cm^{-2} current density. Moreover, the fabricated FWHSC demonstrated its high specific energy density reaching up to 6 W h kg^{-1} (1.5 mW h cm^{-2}) with a power density of 4500 W kg^{-1} (Fig. 5(d)). The remarkable charge storage performance of the fabricated wire-type $\text{NiCo}_2\text{S}_4//\text{ZnCo}_2\text{S}_4$ HSC (1 mW h cm^{-2}) was compared with previous literature reports (more details provided in Table S2, ESI†) on $3\text{D-NiMoO}_4/\text{Ni@CW/rGO/CF}$ device ($0.022 \text{ mW h cm}^{-2}$),³⁰ CuO@CoFe-LDH ($93.75 \text{ } \mu\text{W h cm}^{-2}$),³¹ pErGO@Cuf/Cu wire ($0.039 \text{ mW h cm}^{-2}$).³²

The electrochemical stability and coulombic efficiency results of the designed $\text{NiCo}_2\text{S}_4//\text{ZnCo}_2\text{S}_4$ FWHSC device are shown in Fig. 5(e). The fabricated flexible supercapacitor device demonstrates a capacitance retention of 85.5% along with 98% coulombic efficiency of its original 2000 cycles at a current density of 2 mA cm^{-2} . The inset plot shows the capacitance against current density for the fabricated wire-type $\text{NiCo}_2\text{S}_4//\text{ZnCo}_2\text{S}_4$ FWHSC at different current densities. Impedance analysis in terms of a Nyquist plot of the $\text{NiCo}_2\text{S}_4//\text{ZnCo}_2\text{S}_4$ FWHSC shown in Fig. 5(f) exhibits a capacitive behavior. The inset of the plot shows the equivalent circuit used to fit the impedance dataset. From the fitting dataset, R_s and R_{ct} values were observed to be 11.17 and $12.42 \text{ } \Omega$, respectively, indicating a fast and effective redox kinetic process.²⁶ Further, the normalized capacitance plotted as a function of frequency is provided in the ESI† (Fig. S3). The phase angle plot gives a piece of information about the capacitive or resistive nature of the wire-type $\text{NiCo}_2\text{S}_4//\text{ZnCo}_2\text{S}_4$ FWASC device in the lower to higher frequency region.

Conclusion

In summary, a flexible wire-type $\text{NiCo}_2\text{S}_4//\text{ZnCo}_2\text{S}_4$ hybrid supercapacitor has been fabricated using electrochemically deposited $\text{Cu@CoS}/\text{NiCo}_2\text{S}_4$ and $\text{Cu@ZnCo}_2\text{S}_4$ electrodes on a copper wire. Furthermore, in the three-electrode cell configuration, $\text{Cu@CoS}/\text{NiCo}_2\text{S}_4$ nanostructure exhibited an upgraded areal capacitance value compared to those of the Cu@CoS , $\text{Cu@NiCo}_2\text{S}_4$ and $\text{Cu@ZnCo}_2\text{S}_4$. The porous thin nanosheets

of Cu@CoS/NiCo₂S₄ with a superior electrochemical faradaic charge storage performance (891 F g⁻¹ at 5 mA cm⁻²) showed good reversibility of the material. The fabricated wire-type NiCo₂S₄//ZnCo₂S₄ FWHSC device using KOH/PVA gel electrolyte works over an operating potential window of 1.5 V, and demonstrated an energy density of 6 W h kg⁻¹ and a power density of 4500 W kg⁻¹ with better cyclic stability over 2000 cycles.

Conflicts of interest

There are no conflicts to declare.

Acknowledgements

This study was supported by the National Research Foundation of Korea grant funded by the Ministry of Science and ICT (2020R1A5A8018367), Republic of Korea.

References

- 1 L. Liu, Q. Tian, W. Yao, M. Li, Y. Li and W. Wu, *J. Power Sources*, 2018, **397**, 59–67.
- 2 N. R. Chodankar, S. J. Patil, G. S. R. Raju, D.-W. Lee, D. P. Dubal, Y.-S. Huh and Y.-K. Han, *ChemSusChem*, 2020, **13**(6), 1582–1592.
- 3 L. Yu, H. Zhou, J. Sun, F. Qin, D. Luo, L. Xie, F. Yu and J. Ba, *et al.*, *Nano Energy*, 2017, **41**, 327–336.
- 4 J. Hong, B.-S. Kim, S. Yang, A.-R. Jang and Y.-W. Lee, *J. Mater. Chem. A*, 2019, **7**, 2529–2535.
- 5 W. Liu, M.-S. Song, B. Kong and Y. Cui, *Adv. Mater.*, 2017, **29**, 1603436.
- 6 F. X. Wang, X. W. Wu, X. H. Yuan, Z. C. Liu, Y. Zhang, L. J. Fu, Y. S. Zhu, Q. M. Zhou, Y. P. Wu and W. Huang, *Chem. Soc. Rev.*, 2017, **46**, 6816–6854.
- 7 X. Chu, H. Zhang, H. Su, F. Liu, B. Gu, H. Huang, H. Zhang, W. Deng, X. Zheng and W. Yang, *Chem. Eng. J.*, 2018, **349**, 168–175.
- 8 L. Liu, Y. Feng and W. Wu, *J. Power Sources*, 2019, **410**, 69–77.
- 9 X. Iyu, F. Su and M. Miao, *J. Power Sources*, 2016, **307**, 489–495.
- 10 Q. Gui, L. Wu and Y. Li, *Adv. Sci.*, 2019, **6**, 1802067.
- 11 A. Ramadoss, K.-N. Kang, H.-J. Ahn, S.-I. Kim, S.-T. Ryu and J.-H. Jang, *J. Mater. Chem. A*, 2016, **4**, 4718–4727.
- 12 S. J. Patil, J.-S. Park, Y.-B. Kim and D.-W. Lee, *Energy Technol.*, 2018, **6**, 1380–1391.
- 13 N. R. Chodankar, S.-H. Ji, Y.-K. Han and D.-H. Kim, *Nano-Micro Lett.*, 2020, **1**, 12.
- 14 B. Wei, H. Liang, R. Wang, D. Zhang, Z. Qi and Z. Wang, *J. Energy Chem.*, 2018, **27**, 472–477.
- 15 W. H. Low, P. S. Khiew, S. S. Lim, C. W. Siong and E. R. Ezeigwe, *J. Alloys Compd.*, 2019, **775**, 1324–1356.
- 16 X. Xu, W. Zhong, X. Zhang, J. Dou, Z. Xiong, Y. Sun, T. Wang and Y. Du, *J. Colloid Interface Sci.*, 2019, **543**, 147–155.
- 17 S. Sahoo, T. T. Nguyen and J.-J. Shim, *J. Ind. Eng. Chem.*, 2018, **63**, 181–190.
- 18 S. J. Patil and D.-W. Lee, *J. Micromech. Microeng.*, 2019, **29**, 9.
- 19 C. Zequine, S. Bhoyate, F. Wang, X. Li, K. Siam, P. K. Kahol and R. K. Gupta, *J. Alloys Compd.*, 2019, **784**, 1–7.
- 20 C. Cheng, X. Zhang, C. Wei, Y. Liu, C. Cui, Q. Zhang and D. Zhang, *Ceram. Int.*, 2018, **44**, 17464–17472.
- 21 N. Kurra, C. Xia, M. N. Hedhili and H. N. Alshareef, *Chem. Commun.*, 2015, **51**, 10494–10497.
- 22 S. J. Patil, J. H. Kim and D. W. Lee, *Chem. Eng. J.*, 2017, **322**, 498–509.
- 23 Q. Huang, F. Kang, H. Liu, Q. Li and X. Xiao, *J. Mater. Chem. A*, 2013, **1**, 2418–2425.
- 24 J. Balamurugan, T. D. Thanh, S.-B. Heo, N. H. Kim and J. H. Lee, *Carbon*, 2015, **94**, 962–970.
- 25 X. B. Wang, J. J. Hu, W. D. Liu, G. Y. Wang, J. An and J. S. Lian, *J. Mater. Chem. A*, 2015, **3**, 23333–23344.
- 26 S. J. Patil and D. W. Lee, *J. Mater. Chem. A*, 2018, **6**, 9592–9603.
- 27 S. J. Patil, J. H. Kim and D. W. Lee, *J. Power Sources*, 2017, **342**, 652–665.
- 28 J. Xu, T. Liu, X. Han, S. Wang, D. Liu and C. Wang, *Chem. Commun.*, 2015, **51**, 15819–15822.
- 29 V. Augustyn, J. Come, M. A. Lowe, J. W. Kim, P. L. Taberna, S. H. Tolbert, H. D. Abruña, P. Simon and B. Dunn, *Nat. Mater.*, 2013, **12**, 518.
- 30 L. Naderi and S. Shahrokhian, *J. Colloid Interface Sci.*, 2019, **542**, 325–338.
- 31 Z. Li, M. Shao, L. Zhou, R. Zhang, C. Zhang, J. Han, M. Wei, D. G. Evans and X. Duan, *Nano Energy*, 2016, **20**, 294–304.
- 32 T. Purkait, G. Singh, D. Kumar, M. Singh and R. S. Dey, *Sci. Rep.*, 2018, **8**, 640–653.